Materials Science and Engineering B 278 (2022) 115650

Contents lists available at ScienceDirect

Materials Science & Engineering B

journal homepage: www.elsevier.com/locate/mseb

Effect of stress on the magnetic Barkhausen noise energy cycles: A route for stress evaluation in ferromagnetic materials

Patrick Fagan [a,b], Benjamin Ducharne [b,c,*], Laurent Daniel [d,e,*], Anastasios Skarlatos [a], Mathieu Domenjoud [d,e], Christophe Reboud [a]

[a] CEA, List, Université Paris-Saclay, Palaiseau F-91129, France
[b] Laboratoire de Génie Electrique et Ferroélectricité – INSA de Lyon, Villeurbanne, France
[c] ELyTMaX UMI 3757, CNRS – Université de Lyon – Tohoku University, International Joint Unit, Tohoku University, Sendai, Japan
[d] Université Paris-Saclay, CentraleSupelec, CNRS, Group of Electrical Engineering-Paris (GeePs), 91192 Gif-sur-Yvette, France
[e] Sorbonne Université, CNRS, Group of Electrical Engineering-Paris (GeePs), 75252 Paris, France

ARTICLE INFO

Keywords:
Stress evaluation
Magnetic non-destructive testing
Multiscale model
Hysteresis

ABSTRACT

The analysis of the magnetic Barkhausen noise energy hysteresis cycles, $MBN_{energy}(H)$, is a promising non-destructive testing method for evaluating internal mechanical stresses in ferromagnetic structural steels. This study applies this method to two ferromagnetic materials with significantly different behaviors subjected to uniaxial tensile stress. Coercivity is shown to be the most sensitive tensile stress indicator. A multiscale model is then developed to simulate the stress-dependent $MBN_{energy}(H)$ anhysteretic behavior. Combined with a hysteresis contribution, it successfully reproduces the whole cycle. 2D simulation predictions reveal that the identification of uniaxial tensile stress is more efficient when the magnetic field is applied with an angle between 30° and 75° from the stress direction. The proposed modeling approach allows the prior determination of the most favorable configurations for the sensor orientation depending on the material tested and all available *a priori* knowledge of the stress configuration.

1. Introduction

Mechanical internal stresses are a determinant factor to material performance, structural integrity, and lifetime of industrial systems. Many techniques have been developed for their evaluation [1,2]. The hole-drilling method [3], the contour method [4], the crack compliance method [5], or the stripping method [2] are the most common mechanical techniques [1]. Chemical methods [2] can also be found. These mechanical and chemical techniques, however, are destructive.

Non-destructive testing (NDT) methods for evaluating the internal mechanical stresses have also been developed [6-8]. They include diffraction methods (X-ray, Neutron), ultrasonic methods, or acoustic emission [9]. These techniques can be applied successfully independently of the nature of the tested specimen. In the specific case of conductive and/or ferromagnetic materials, magnetic NDT techniques are available. Their applicability is more limited, but they offer many advantages such as fast response, low cost, small size, and easy maintenance.

Eddy currents testing [10], magneto-acoustic emission [11,12], electromagnetic acoustic transducer [2], and Magnetic Barkhausen Noise (MBN) [13-15] are some of the most used magnetic methods, alone or in combination with other NDT techniques [16]. This paper focuses on the use of MBN signals to detect stress in ferromagnetic materials.

Ferromagnetic materials exhibit a complex magnetic domain microstructure. The modification of this magnetic domain microstructure under the influence of an external stimulus (magnetic field, mechanical stress, or temperature variation) generates unpredictable and discontinuous domain wall motions, including successively pinning phases and large amplitude displacements [17,18]. MBN signal is an indirect reflection of this microstructural reorganization. It is linked to the magneto-mechanical state and the material properties [19]. MBN is a stochastic process, and MBN raw measurements are not reproducible in practice. Their analysis is usually performed through time-

* Corresponding authors at: Laboratoire de Génie Electrique et Ferroélectricité – INSA de Lyon, Villeurbanne, France (B. Ducharne) Université Paris-Saclay, CentraleSupelec, CNRS, Group of Electrical Engineering-Paris (GeePs), 91192 Gif-sur-Yvette, France (L. Daniel).
E-mail addresses: patrick.fagan@insa-lyon.fr, patrick.fagan@cea.fr (P. Fagan), benjamin.ducharne@insa-lyon.fr (B. Ducharne), laurent.daniel@centralesupelec.fr (L. Daniel), Anastasios.SKARLATOS@cea.fr (A. Skarlatos), mathieu.domenjoud@centralesupelec.fr (M. Domenjoud), Christophe.REBOUD@cea.fr (C. Reboud).

https://doi.org/10.1016/j.mseb.2022.115650
Received 13 June 2021; Received in revised form 8 December 2021; Accepted 3 February 2022

independent indicators such as the Root Mean Square (RMS) [19], the $MBN_{envelope}$ [20], or the MBN_{energy} [21-24].

Many scientific works have described the use of MBN for the evaluation of residual mechanical stresses in ferromagnetic materials [13]. Even if the first ones have been published at the beginning of the 20th century [25], it is still a timely subject, and the number of recent publications [26-38] is very high. Whatever the MBN indicator monitored, a preliminary calibration step is usually required. Non-destructive (X-ray diffraction [1,2], strain gauges [39]) or destructive (Vickers impact [38], hole drilling [2,3]) methods can be used for this calibration.

MBN measurements can provide information up to several hundreds of μm under low-frequency excitation (<1 Hz) [40]. Accurate surface inspections can be obtained with much higher frequencies (>100 Hz) [40].

Several indicators have been used for the estimation of residual stress: $MBN_{envelope}$ [20], RMS value [14,15], MBN_{energy} [23], or statistical markers, including the number of avalanches [28]. The relation between mechanical stress and MBN is nonlinear and is affected by plastic deformation and fatigue [31]. Most of the time, empirical relations are used [28,31]. However, numerical simulations based on magneto-elasticity [31,36] or stochastic approaches [37] have also been developed to interpret the mechanisms behind these empirical relations. For example, a linear relationship between the reciprocal of the $MBN_{envelope}$ peak amplitude and the residual stress is established in [41]. However, the slope of this linear fit is identified from measurement since its theoretical determination would require delicate calculations and precise knowledge of the magnetostrictive behavior [41].

Although the stress state in industrial parts is usually multi-axial, the multiaxiality of stress is seldom considered in MBN studies [29,42]. Similarly, material anisotropy and its influence on MBN and stress evaluation are usually ignored. Material anisotropy, however, can be considered by controlling the magnetic excitation direction (rotating magnetic field [26,34] or inductor [43,44]) or controlling MBN measurement direction (directional sensor [45]).

This work aims to establish a modeling framework for the effect of stress on MBN and reach a quantitative understanding of stress evaluation. This work follows the footsteps of a recent modeling approach for the description of MBN [23,46]. MBN is studied through the $MBN_{energy}(H)$ hysteresis cycles simulated by combining an anhysteretic behavior and a hysteresis contribution. Compared to the previous contribution [23], the modeling approach is now capable of describing the effect of mechanical stress on the MBN response.

In the domain of mechanical stress evaluation, a unified theory relating magnetic signals to basic magnetic parameters is still lacking. This study undertakes the first steps toward an alternative method involving the combination of a predictive simulation tool and experimental observations. The validity range of classical MBN models is usually limited to the experimental conditions used for parameter identification. The approach proposed in this paper allows foreseeing stress distribution and Barkhausen noise-related behaviors in much more general configurations.

The experimental measurement of stress-dependent MBN signal is first performed on two materials (section 2), chosen for their high difference in crystalline anisotropy and crystallographic texture. Section 3 describes the modeling approach and its extension to consider the effect of stress. In the last section, measurements and simulations are compared, and the potentialities of MBN_{energy} measurements for stress detection are discussed.

2. Experimental characterization of the $MBN_{energy}(H)$ and $B(H)$ hysteresis cycles

2.1. Materials

Two materials have been chosen for this work based on their different material properties connected with the magnetization process. The magnetization process in ferromagnetic materials is the result of two distinct mechanisms. The first mechanism is domain wall motion. The magnetic domains with a magnetization oriented favorably to the applied magnetic field grow, while the domains unfavorably oriented decline in proportion. The second mechanism is magnetization rotation. The magnetization of a magnetic domain, initially oriented along an easy axis, coherently rotates towards the direction of the applied magnetic field. The magnetization process is schematically illustrated in Fig. 1.

The first material is a Grain Oriented Iron Silicon steel (GO FeSi), typically used in transformer cores [47,48]. It contains 3 wt% silicon. It is characterized by a strong crystallographic texture and a high crystalline anisotropy, resulting in a substantial macroscopic anisotropy. Due to the Goss texture, most grains in the material have an easy direction ($\langle 100 \rangle$) close to the rolling direction (RD). As a result, the magnetization rotation mechanism is almost absent in this material when it is magnetized along RD. The domain wall motions mainly drive the magnetization. The saturation state is made of domains with magnetization along the easy direction parallel (or very close) to RD.

The second material is a high yield strength (of the order of 1000 MPa) Iron-Cobalt alloy (FeCo), typically used for high-performance rotating machines [49,50]. The composition is 49% Fe, 49% Co and 2 % V. The material exhibits an isotropic behavior in the sheet plane. The crystallographic texture is not very pronounced, and the magneto-crystalline anisotropy is weak. This results in a more prominent role of the magnetization rotation mechanism in the magnetization process.

The dimensions of the GO FeSi and FeCo specimens studied are given in Fig. 2 below:

2.2. Characterization setup

The objective is to characterize both the $MBN_{energy}(H)$ and the standard $B(H)$ magnetic responses of a specimen subjected to uniaxial tensile stress. It requires performing a magnetic measurement while constant stress is applied. A 2D view of the setup is depicted in Fig. 3 below:

2.2.1. Mechanical stress

A tension–compression machine (Zwick/Roell Z030) and the associated computer are used for the stress application [51]. A 10 kN load cell (strain gauge sensor TC-LC010kN) is used for the force measurement. The resolution and accuracy of the force and displacement sensors are 0.2 N ± 0.06% and 1 μm ± 0.1%, respectively. The first series of measurements was done by increasing incrementally ($\Delta\sigma = 5$ MPa) the mechanical force up to 100 MPa for the GO FeSi and 500 MPa for the FeCo (far below the yield strength for each material). At each increment, the stress was maintained constant for the duration of the magnetic measurement. For the second series, the mechanical stress was decreased with the same force step, down to complete stress cancellation. Both the sequences were repeated to check the reproducibility.

2.2.2. Magnetic excitation

The magnetic part is made of two U-shaped FeSi 3% yokes, ensuring the closure of the magnetic flux. The tested specimen is placed and kept inside the testing machine thanks to a diamagnetic fixture (see Fig. 3). A series circuit of two primary coils (16 AWG wire), one wound around each yoke (672 turns each) and supplied in current by a Kepco 72-14MG amplifier, ensure the magnetic field generation. This power amplifier can generate 14 A and 72 V, with 0.2% accuracy. It is driven by a National Instrument DAQ USB-6346 acquisition device. The sampling frequency is 500 kHz for all channels.

2.2.3. Magnetic instrumentation

The tangent magnetic field H is measured locally on the surface of the tested specimens using a GM08 Gaussmeter and a transverse Hall probe. The accuracy of this sensor is 1%, and the noise level is close to ± 40

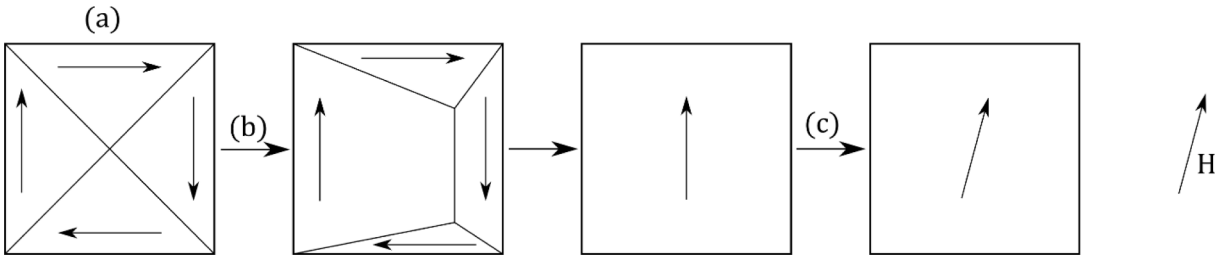

Fig. 1. Schematic illustration of the magnetization process. (a) Demagnetised state (b) Domain wall motion (c) Magnetisation rotation. In practice, the two mechanisms can occur simultaneously.

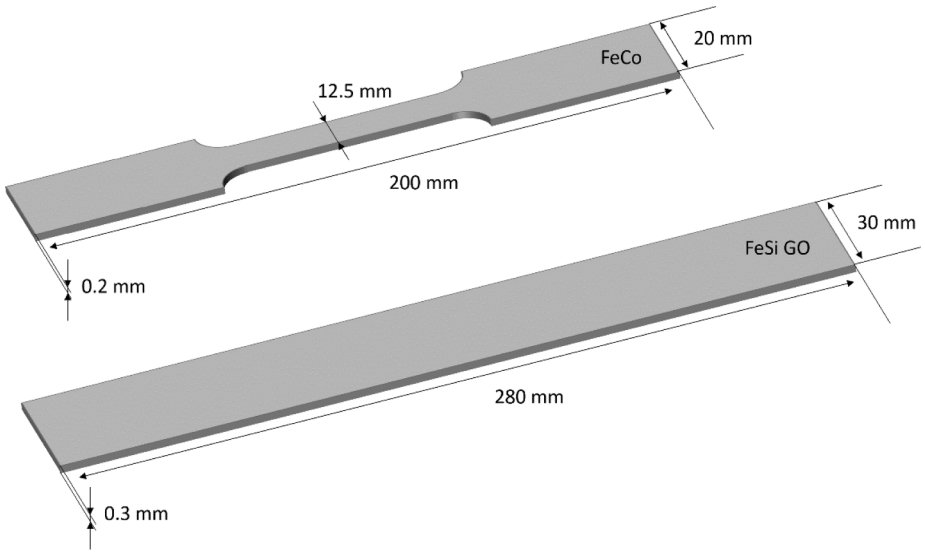

Fig. 2. Dimensions of the GO FeSi and FeCo specimens tested.

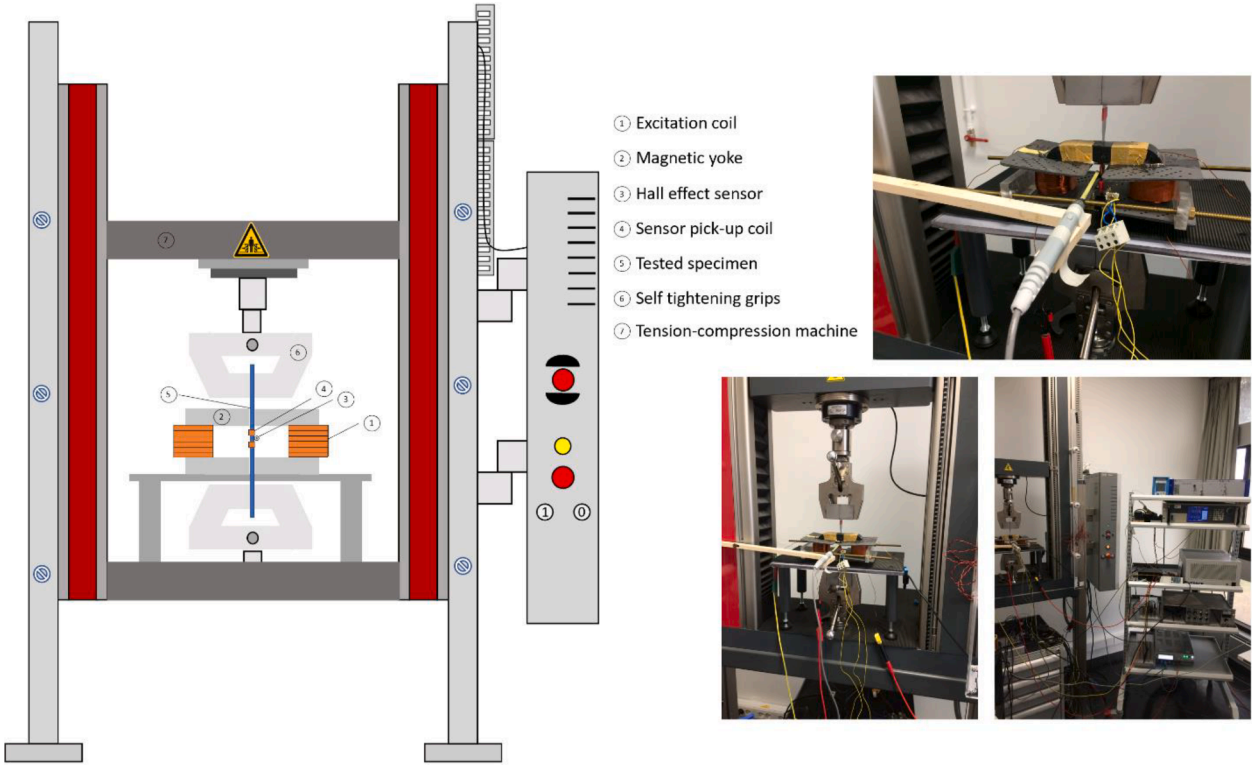

Fig. 3. Overall 2D view of the experimental setup for measuring the stress dependent *MBN and magnetic responses of ferromagnetic specimens*.

$A{\cdot}m^{-1}$. All the tested specimens are wound with two 100-turns coils, in opposite directions, as described in [52]. The voltage drop over a single coil due to the low-frequency variations is monitored as well. Both these differential and common-mode measurements are done simultaneously to acquire the time-dependent MBN and magnetic flux variations. The Differential method for the MBN raw signal acquisition leads to a high reduction of the parasitic noises and interferences affecting the two pick-up coils quasi simultaneously.

The $B(H)$ loop is obtained by numerical integration of the common mode. A numerical correction is done to cancel the undesired drift due to the integration process.

2.3. MBN energy

As the domain wall motions are a stochastic process, the MBN raw signal is unpredictable and not reproducible. To overcome this issue and converge towards repeatable results, time average indicators are used for the MBN analysis. Here, the MBN_{energy} is chosen. It is defined as [23,53]:

$$MBN_{energy}(t) = \int_0^t sign\left[\frac{dH}{dt}(s)\right] V_{BK}^2(s)ds \quad (1)$$

where V_{BK} is the electromotive force measured from the coil sensor. The construction of the MBN_{energy} hysteresis loop from the raw MBN measurement is illustrated in Fig. 4.

The MBN_{energy} is not *stricto sensu* an energy, but as described in [23], it can be considered an image of the kinetic energy of domain walls. To compare the $MBN_{energy}(H)$ and the standard $B(H)$ hysteresis loops, it is necessary to renormalize the MBN_{energy} measurement. This renormalization can be achieved by equalizing the hysteresis area between the two measurements or equalizing the measured values at the beginning of the saturation elbow. However, in an NDT situation where $B(H)$ hysteresis loops are most of the time unavailable, this renormalization process is impossible and is replaced by a normalization to one.

In practice, during the experimentation, the MBN_{energy} quantity is returned through an analogic procedure, including:

- an amplification of the raw MBN signal (G = 50 dB)
- a band-pass filter (MAX274ACN analogic filter). The cut-off frequencies were set to 4 and 12 kHz, and the filter response attenuation slope to 70 dB/dec.
- an AD633 analog multiplier.
- A low noise operational amplifier LT1001 in an integrator setup and an external switch push button to reset the integration process at the beginning of each new measurement.

For a reduction of the parasitic noises, all the data were averaged over five periods of excitation.

2.4. Experimental results

The $B(H)$ and the $MBN_{energy}(H)$ hysteresis loops obtained for the GO FeSi specimen are shown in Fig. 5 for three different levels of tensile stress.

The $B(H)$ and the $MBN_{energy}(H)$ hysteresis loops obtained for the FeCo specimen are shown in Fig. 6 for three different tensile stress levels.

A first observation is that the magnetic behavior of the FeCo is much more sensitive to the application of tensile stress compared to the GO FeSi. A tensile stress increases the permeability at low field for the two materials tested. It is consistent with classical observations on positive magnetostriction materials [17,54]. The tensile stress also reduces the coercivity. This effect is also consistent with previous observations [50,55], and it is much more significant for the FeCo alloy. For both materials, the tensile stress decreases the slope in the saturation/remanence branch.

Unlike the FeCo, the MBN energy cycles for the GO FeSi exhibit a very similar shape compared to the $B(H)$ loop. This observation is consistent with the fact that only the domain wall motions contribute to the $MBN_{energy}(H)$ hysteresis cycles, as described in [23]. The magnetic behavior of the GO FeSi being mostly driven by domain wall motion, the

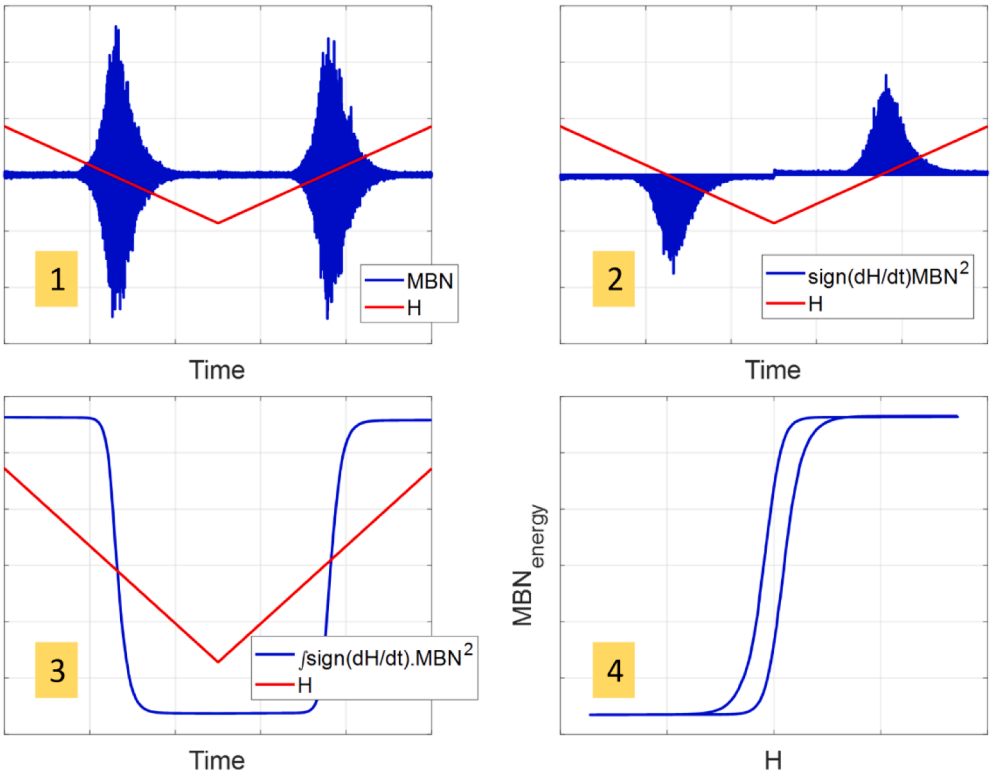

Fig. 4. $MBN_{energy}(H)$ hysteresis loop, construction process.

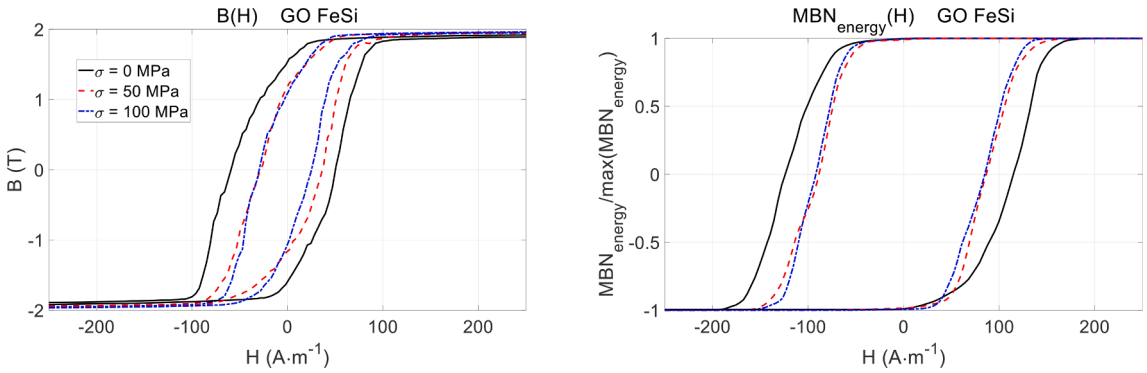

Fig. 5. GO FeSi: experimental measurement for the stress-dependent *B(H)* - left - and $MBN_{energy}(H)$ hysteresis cycles.

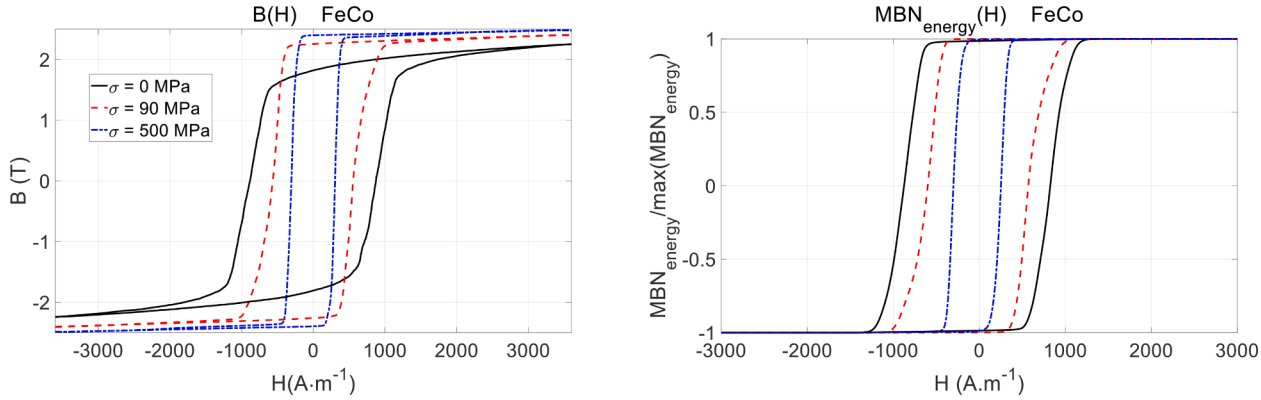

Fig. 6. FeCo: experimental measurement for the stress-dependent *B(H)* - left - and $MBN_{energy}(H)$ hysteresis cycles.

B(H) and $MBN_{energy}(H)$ curves are the images of the same processes. On the contrary, magnetization rotation is more prominent for the FeCo. The *B(H)* curve incorporates physical mechanisms absent from the $MBN_{energy}(H)$ curves. It is then expected that they show more significant differences.

It is also worth noting that increasing tensile stress tends to make the $MBN_{energy}(H)$ and *B(H)* cycles more similar, which could be interpreted as a lesser contribution of rotation mechanism in tension strained specimens.

A good indicator of the effect of stress on the magnetic behavior is the coercive field H_c. Fig. 7 shows the coercive fields extracted from the *B(H)* measurements and the $MBN_{energy}(H)$ measurements, for both materials.

A shift can be observed between these two extractions, even though the magnetic field is obtained from the same sensor. This difference is due to the filtering step performed to detect the MBN noise, which

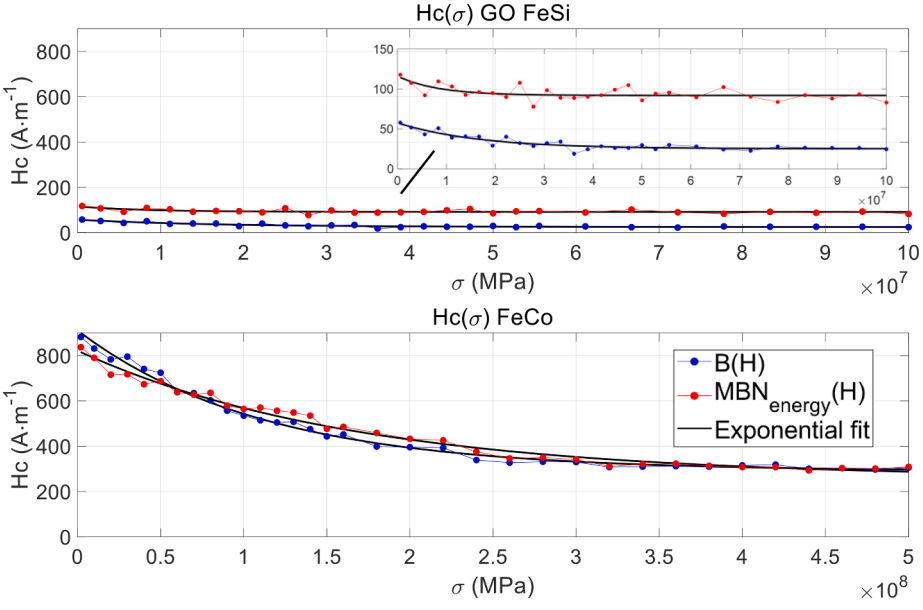

Fig. 7. Stress dependence of the measured *B(H)* and $MBN_{energy}(H)$ coercivities.

affects the value of the magnetic field. This effect is more visible for the FeSi GO, which exhibits a much lower coercivity. The frequency analysis (Fig. 8) of the analytical filter confirms this statement. The magnitude plot shows (as expected) 4 and 12 kHz as cut-off frequencies, while the phase plot reveals a phase answer varying from 6 to −12 rd. The phase is negative for $f > 6$ kHz, which is a large majority of the bandwidth. This negative phase shift is significant enough to delay the Barkhausen measurement and increase the $MBN_{energy}(H)$ coercivities.

From Fig. 7, it is observed that the coercivity of the GO FeSi is almost insensitive to the application of tensile stress, while the FeCo shows more sensitivity. The evolution of the coercive field H_c under uniaxial tensile stress can be approximated by a decreasing exponential function in the form of Eq. (2).

$$H_c(\sigma) = a.e^{b\sigma} + c \tag{2}$$

The MATLAB® curve fitting toolbox was used to identify the parameters a, b and c from the results shown in Fig. 7. These parameters are given in Table 1.

For some materials, the measurement of $H_c(\sigma)$ could be an excellent macroscopic indicator to evaluate the level of stress in a material [56]. However, to obtain a more comprehensive description of the effect of stress on the magnetic signature of ferromagnetic materials, we are developing in the next section a modeling approach for the $B(H)$ and $MBN_{energy}(H)$ loops.

3. Modelling approach

The choice of modeling approach presented here is based on the classical separation between reversible (anhysteretic) and irreversible (hysteretic) contributions to magnetic behavior. The overall behavior will be defined as the superimposition of an anhysteretic term with a hysteresis contribution. The approach was presented in [23] for a purely magnetic loading and is extended hereafter to the case where a mechanical stress is applied.

3.1. Anhysteretic behavior: The multiscale model

The multiscale model [57,58] has initially been developed to describe the anhysteretic magnetic behavior of a ferromagnetic specimen based on the statistical evolution of its domain microstructure. The multiscale model provides directional information and naturally includes anisotropy effects [59]. A polycrystalline ferromagnetic specimen is described as an aggregate of single crystals (grains). Each grain is divided into a finite number of magnetic domain families. Each family is characterized by a given magnetic orientation α. The volume fraction f_α of each magnetic domain family is calculated using their potential energy W_α:

Table 1
Parameters a, b, and c for the description of $H_c(\sigma)$ as defined in Eq. (2).

		a	b	c
FeCo	***B(H)***	620.9	$-9\ 10^{-9}$	290.4
	MBN$_{energy}$(H)	562.2	$-6\ 10^{-9}$	259.7
		a	b	c
FeSi	***B(H)***	32.4	$-6\ 10^{-8}$	25.05
	MBN$_{energy}$(H)	23.83	$-1.2\ 10^{-7}$	91.84

$$W_\alpha = W_\alpha^K + W_\alpha^H + W_\alpha^\sigma \tag{3}$$

$$W_\alpha^K = K_1\left(\gamma_1^2\gamma_2^2 + \gamma_2^2\gamma_3^2 + \gamma_3^2\gamma_1^2\right) + K_2\gamma_1^2\gamma_2^2\gamma_3^2 \tag{4}$$

$$W_\alpha^H = -\mu_0 \mathbf{H}_\alpha.\mathbf{M}_\alpha \tag{5}$$

$$W_\alpha^\sigma = -\boldsymbol{\sigma}_\alpha : \boldsymbol{\varepsilon}_\alpha^\mu \tag{6}$$

$$f_\alpha = \frac{\exp\left(-A_S\ W_\alpha\right)}{\sum_\alpha \exp\left(-A_S\ W_\alpha\right)} \tag{7}$$

where ${W_\alpha}^k$, ${W_\alpha}^H$, ${W_\alpha}^\sigma$, stands for the magneto-crystalline (Eq. (4)), magnetostatic (Eq. (5)), and magneto-elastic (Eq. (6)) energy, respectively. $\mathbf{H}_\alpha$, $\mathbf{M}_\alpha$, $\boldsymbol{\sigma}_\alpha$ and $\boldsymbol{\varepsilon}_\alpha^\mu$ are the magnetic field, the magnetization, the stress tensor, and the magnetostriction strain tensor defined at the magnetic domain scale. $\mathbf{M}_\alpha$ is defined by its norm (the material saturation magnetization M_s), and its direction is given by γ_1, γ_2, γ_3. $\boldsymbol{\varepsilon}_\alpha^\mu$ is defined by the magnetostriction constants λ_{100} and λ_{111} [57]. K_1 and K_2 are the magneto-crystalline energy constants. A_S is a material parameter that can be set using the initial macroscopic susceptibility χ^0 of the unstressed anhysteretic magnetization curve [57].

Once f_α calculated for all magnetic domains families, the magneto-elastic response at the grain scale is obtained by a volume average:

$$\boldsymbol{\varepsilon}_g^\mu = \langle \boldsymbol{\varepsilon}_\alpha^\mu \rangle = \sum_\alpha f_\alpha \boldsymbol{\varepsilon}_\alpha^\mu \tag{8}$$

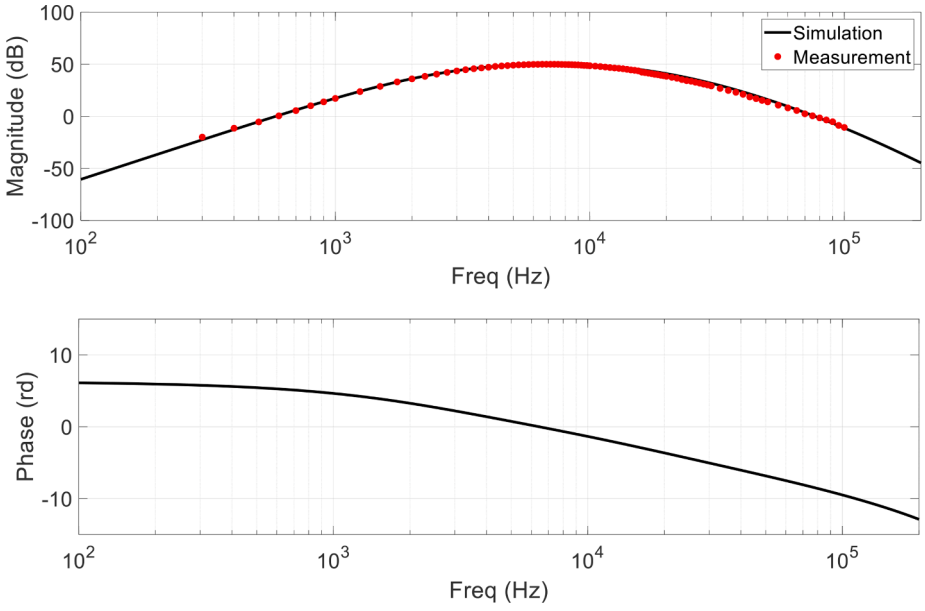

Fig. 8. MAX274ACN analogic filter Bode plots, comparison measurement/simulation.

$$\mathbf{M}_g = \langle \mathbf{M}_\alpha \rangle = \sum_\alpha f_\alpha \mathbf{M}_\alpha \tag{9}$$

Finally, an orientation distribution function (distribution of the crystallographic orientations) obtained from X-ray diffraction or Electron Back Scattering Diffraction (EBSD) is used to simulate the behavior at the polycrystalline scale.

In the simplified calculation process used here, both the magnetic H and mechanical $\boldsymbol{\sigma}$ external stimuli are supposed to be uniform within the material. The potential energy and the volume fraction of each magnetic domain family are calculated first. Then, the magnetization is calculated for each grain (Eq. (9)), and finally, an average over the volume is performed to obtain the whole specimen magnetization:

$$\mathbf{M} = \langle \mathbf{M}_g \rangle \tag{10}$$

This process allows the construction of the stress-dependent anhysteretic magnetization curves based on a limited number of intrinsic material parameters. They have to be complemented with the crystallographic texture data to predict the macroscopic material behavior. The magnetic induction is finally easily deduced from the magnetization using Eq. (11).

$$\mathrm{B} = \mu_0 (H + M) \tag{11}$$

In all the following, the simulation parameters and the crystallographic texture data from [48] and [60] will be used for the GO FeSi and the FeCo, respectively. The orientation distribution function consists of 60 orientations for GO FeSi (strong texture) and 650 for FeCo (almost isotropic). The material parameters are given in Table 2 below:

3.2. B(H) hysteresis loops

From the knowledge of the stress-dependent anhysteretic magnetization curve, the full hysteresis must now be constructed. A popular approach is the Jiles-Atherton model [61-65]. Given the shape observed for the hysteresis loops, and given the fact that we are only dealing with major loops, we have opted for a simple hysteresis shift from the anhysteretic curve to the hysteresis loop. This approach is analogous to a mechanical dry-friction [66-68]. The $B(H)$ loop is then defined as:

$$B = f_{anhyst}(H + \delta H_c(\sigma)) \tag{12}$$

where $H_c(\sigma)$ is the stress-dependent function for the coercivity (Eq. (2) is only valid under tensile stress ($\sigma > 0$)) and $\delta = \pm 1$ a directional parameter.

$$\begin{aligned} \delta &= 1 \quad if \quad \frac{dH}{dt} > 0 \\ \delta &= -1 \quad if \quad \frac{dH}{dt} < 0 \end{aligned} \tag{13}$$

Fig. 9 below depicts some comparisons between simulations and experimental results for both materials tested with and without tensile stress. The excellent agreement is considered a validation of the simulation method.

3.3. $MBN_{energy}(H)$ hysteresis loops

The adoption of a similar approach for the MBN_{energy} loops requires some adjustment. Indeed, it is reminded that domain wall motion is the only magnetization contribution observed through the MBN_{energy} measurements. The simulation of the anhysteretic $MBN_{energy}(H)$ behavior is possible with the multiscale model, but it requires restricting the magnetization process to the domain wall contribution. This is done by setting K_1 and K_2 (the magneto-crystalline anisotropy coefficients) with exaggerated values [23]. A "no-rotation" anhysteretic magnetization curve is obtained and used as the skeleton for the MBN_{energy} curve. As explained in [23], the hysteresis shift is considered the same for the $MBN_{energy}(H)$ and the $B(H)$ hysteresis cycles. Therefore, the parameters defined for the $B(H)$ curve are equally set for the $MBN_{energy}(H)$ curve :

$$MBN_{energy} = f_{anhyst}^{no\ \ rotation}(H + \delta H_c(\sigma)) \tag{14}$$

The MBN_{energy} curve can finally be normalized to one as described in the first section for comparison with the experimental measurements.

These comparisons are presented in Fig. 10. Except in the saturation elbow, good agreement is observed here once again.

Table 2
Multiscale model simulation parameters for the GO FeSi and the FeCo.

Coefficient	M_s	K_1 ; K_2	λ_{100} ; λ_{111}	A_s
Unit	$A.m^{-1}$	$kJ.m^{-3}$	–	m^3J^{-1}
FeSi GO	$1.61\ 10^6$	38 ; 0	$23\ 10^{-6}$; $-4.5\ 10^{-6}$	$2\ 10^{-2}$
FeCo	$1.91\ 10^6$	2 ; 0	$101\ 10^{-6}$; $27\ 10^{-6}$	$3\ 10^{-3}$

4. Feasibility of a stress evaluation technique based on MBN measurement

The evaluation of mechanical stress in structural ferromagnetic steel is fundamental. It allows anticipating undesired degradation and failure. As illustrated in Fig. 10, MBN is highly stress-dependent. It is well adapted to modern NDT as it can be implemented with limited costs and space restrictions. It is shown in this section that the proposed approach for the modeling of MBN_{energy} can be an efficient tool to optimize stress evaluation strategies using MBN measurements. It is worth noting that such evaluation would require specific inversion procedures, which are not discussed in this paper focused on the effect of stress on the MBN signals.

4.1. Evaluation of tensile stress configurations

The first case considered is a configuration of tension stress as considered in the experiments performed in this paper. The effect of stress on the coercive field, obtained either from the experimental $MBN_{energy}(H)$ or from the $B(H)$ hysteresis cycles, was shown in Fig. 7. Other indicators can be used, such as the $MBN_{energy}(H)$ hysteresis area, or the magnetic field H_{95} measured at $MBN_{energy} = 0.95 \times \max(MBN_{energy})$ or H_{99} measured at $MBN_{energy} = 0.99 \times \max(MBN_{energy})$. These indicators are reported in Fig. 11 as a function of the applied stress. They have been normalized with their value at $\sigma = 0$.

The dependence to tensile stress is clear for the FeCo but less significant for the GO FeSi. All indicators exhibit similar trends with increasing stress level. The effect of uniaxial stress on the coercive field is correctly described by Eq. (2) (as shown in Fig. 7), but it requires previous calibration on experimental results. Moreover, no generalization to more complex mechanical loading can be expected since it is the result of a purely mathematical fitting. H_{95} and H_{99} on the other hand can be predicted independently from the measurement using the proposed multiscale approach. The results are shown in Fig. 12 for these two indicators, both for GO FeSi and FeCo.

Fig. 12 shows a clear decrease of H_{95} and H_{99} with the application of stress and a saturation of this effect at very low stress. Although the trend is consistent with experimental results, the quantitative differences are significant. This disagreement can notably be explained by the difference between the anhysteretic function (used in the exploitation of the modelling results) and the increasing and decreasing part of the hysteresis cycle envelope (used in the exploitation of the experimental results). Together with relatively low variations, it makes the direct use of the model uneasy in this configuration. However, the modelling approach can be used to explore the effect of different sensor orientations. Fig. 13 shows, in polar coordinates and for the FeCo alloy, the predicted normalized H_{95} and H_{99} indicators for a uniaxial stress applied along the rolling direction (RD), as a function of the orientation of the MBN sensor at various angles from the rolling direction (RD, 0°) to the

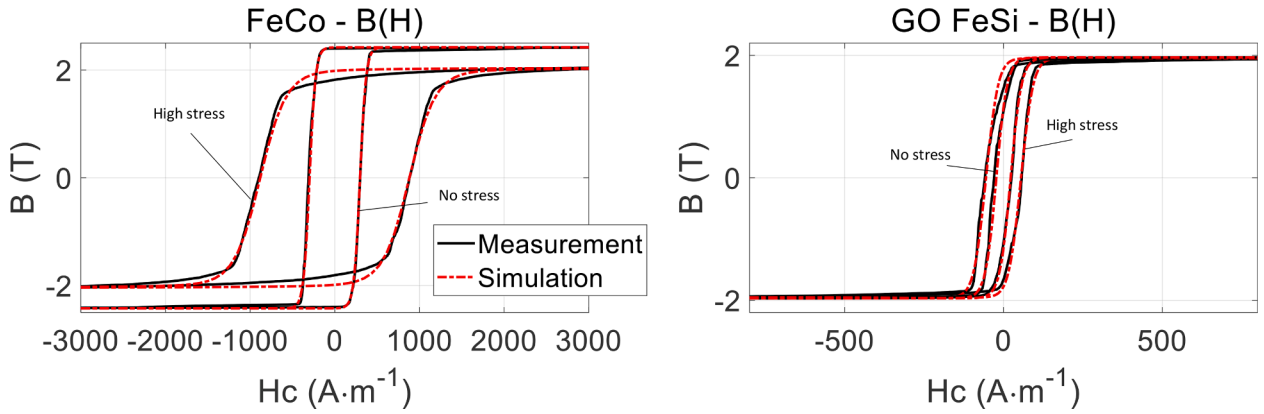

Fig. 9. Comparisons simulations/measurements for the *B(H)* hysteresis cycles.

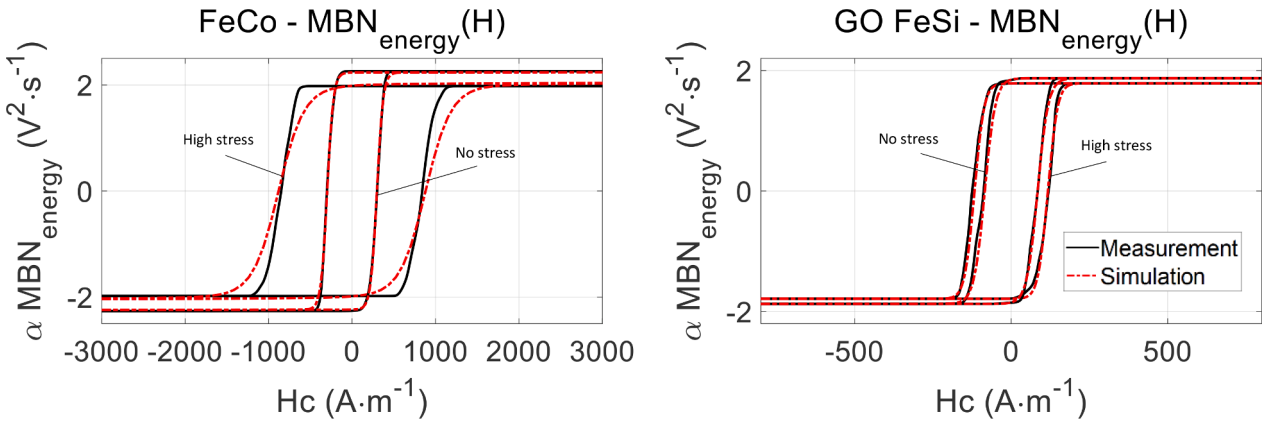

Fig. 10. Comparisons simulations/measurements for the $MBN_{energy}(H)$ hysteresis cycles.

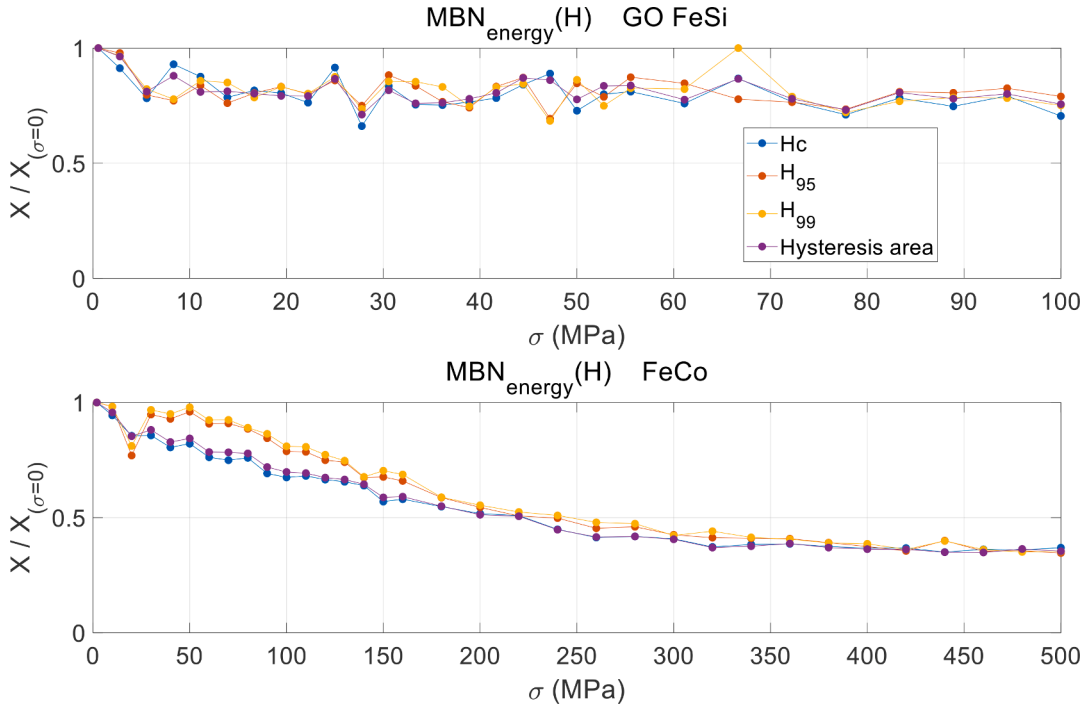

Fig. 11. Tensile stress dependence of the $MBN_{energy}(H)$ hysteresis area, coercive field, H_{95}, and H_{99} normalized by the corresponding stress-free reference.

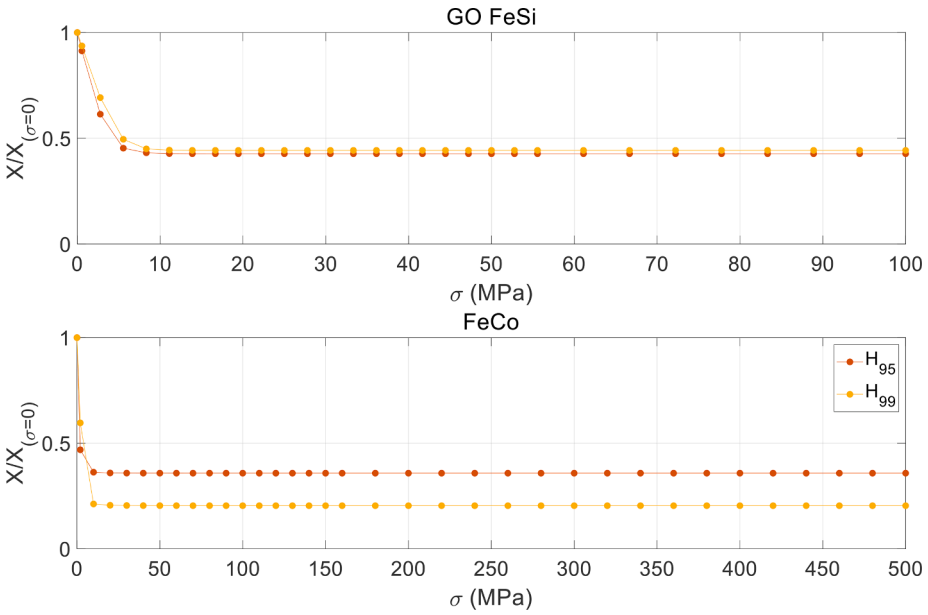

Fig. 12. Multiscale model prediction H_{95} and H_{99} normalized by the corresponding stress-free reference, as a function of the applied tensile stress.

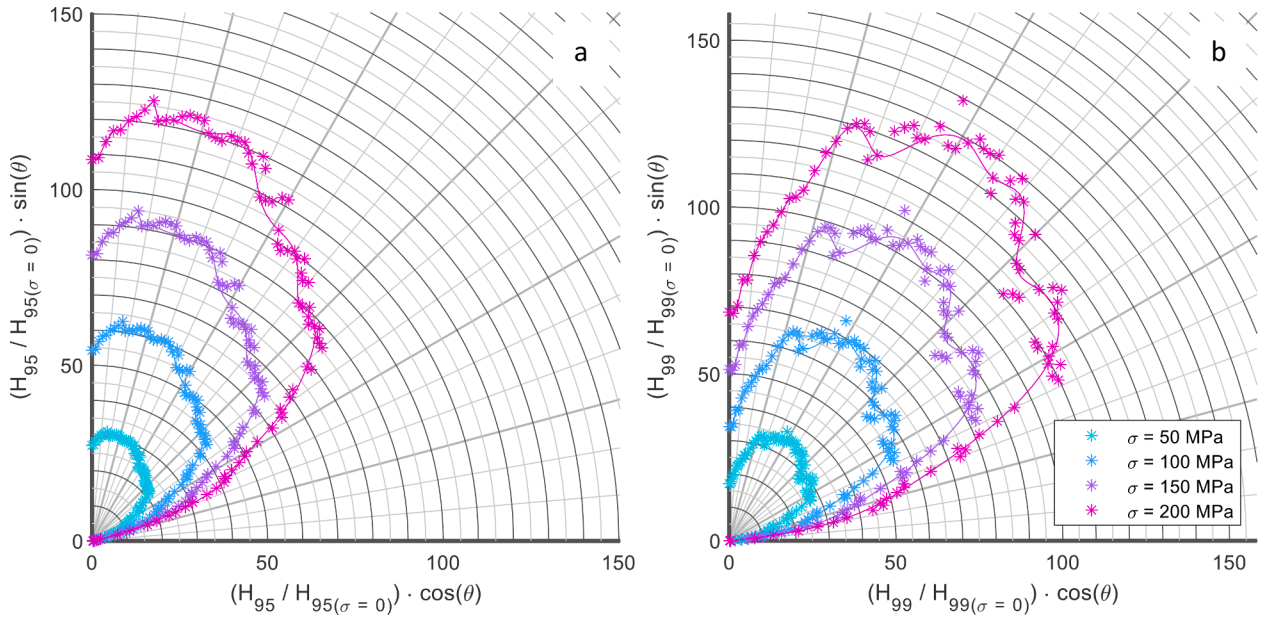

Fig. 13. FeCo alloy: Evolution of the predicted normalized (a) H_{95} and (b) H_{99} indicators under 50, 100, 150, and 200 MPa tensile stress applied along RD as a function of the orientation of the MBN sensor from RD to TD. The dots show the calculation results, while the lines guide the eyes.

transverse direction (TD, 90°). The results are not perfectly smooth because a discrete orientation distribution function (650 crystallographic orientations) has been used to describe the crystallographic texture, so that the angular response of the material is not exactly regular. The general trend is given by a spline approximation shown as a plain line.

While it is evident that slight variation is observed when the MBN sensor is aligned with the applied stress (RD), much more significant variations are found when the sensor is positioned perpendicularly to TD. It is also found that the optimal orientation for maximum MBN sensitivity is obtained when the magnetic field is applied with an angle between 30° and 75° from RD. Our experimental setup and samples allow only a measure with the magnetic field aligned with RD, hence experimental validation of these results has not been done. The required setup would be similar to the one described in [14] and the use of a biaxial stress device (as in [69]).

In a practical application, if the orientation of the uniaxial stress is known before its detection, the modeling can be used to choose the most sensitive orientation for the sensor. On the contrary, if the orientation of the uniaxial stress is unknown, several successive measurements can allow the identification of both intensity and orientation.

4.2. *Evaluation of multi-axial stress configurations*

Most practical industrial parts are subjected to a multi-axial stress state and not only uniaxial tension. For an effective evaluation of stress, it is necessary to generalize the MBN 1D analysis to the real-life 3D multi-axial stress configurations. There are few experiments in the scientific literature that establish the link between magnetic response and multi-axial stress [69-74]. Unfortunately, none of them report MBN

observations. The multiscale modeling approach proposed in this study is another way to explore the influence of multi-axial stress on the $MBN_{energy}(H)$ hysteresis cycles. Even though it has been parameterized and validated for a 1D tensile stress configuration, the model is intrinsically 3D.

As an example, Fig. 14 shows the modeling results obtained for H_{95} (very similar results are obtained for H_{99}) in the case of the FeCo sample subjected to a biaxial stress. RD and TD are the principal axes for the stress, and the MBN sensor is aligned along RD. The stress tensor $\boldsymbol{\sigma}$ is given by Eq. (15) in the (RD, TD) coordinate system and the principal stresses σ_{xx} and σ_{yy} vary from −250 to 250 MPa.

$$\boldsymbol{\sigma} = \begin{pmatrix} \sigma_{xx} & 0 & 0 \\ 0 & \sigma_{yy} & 0 \\ 0 & 0 & 0 \end{pmatrix}_{RD,TD,z} \tag{15}$$

The results confirm again that a configuration with an MBN sensor positioned parallel to the direction of a uniaxial tension is the less sensitive configuration: the indicator H_{95} shows almost no variation on the horizontal line at $\sigma_{yy} = 0$ for $\sigma_{xx} > 0$. On the contrary, biaxial configurations with a compressive component parallel to the MBN sensor create the most significant variation of H_{95}. It is again concluded that if the stress configuration is known *a priori*, the multiscale approach can be used to define the most appropriate orientation of the MBN sensor for maximum sensitivity in stress evaluation.

5. Conclusion

The stress dependence of $B(H)$ and $MBN_{energy}(H)$ hysteresis loops exhibit apparent similarities. $MBN_{energy}(H)$ hysteresis cycles can be modeled by combining an anhysteretic behavior and a hysteresis contribution. On the one hand, the anhysteretic contribution can be calculated using a multiscale approach. On the other hand, the hysteresis contribution can be kept identical to the one identified from the standard B(H) loops for a given specimen. In this paper, this simulation approach has been investigated to analyze the potentialities of MBN techniques to detect mechanical stress in ferromagnetic materials. It is successfully applied on two exemplary ferromagnetic materials with significantly different behavior (an Iron-Silicon steel and an Iron-Cobalt alloy) subjected to uniaxial tensile stress. Several indicators have been tested for their sensitivity to stress. Based on $MBN_{energy}(H)$ analysis, coercivity appears as a good indicator for both materials. Two other indicators, easily predicted by the proposed modeling approach, H_{95}, and H_{99}, have also shown interesting stress dependence, especially when the magnetic rotation mechanism is significant (FeCo).

The simulation method has further been used to investigate the MBN variations of the Iron-Cobalt alloy under various sensor configurations and multi-axial stress states. It is concluded that the proposed approach can be a great help in the definition of optimal MBN sensor positioning depending on the stress configuration. It is also shown that uniaxial tension is one of the most unfavorable configurations for stress detection, although appropriate sensor positioning can increase measurement sensitivity.

This work is a leap forward to the understanding and modeling of magnetization mechanisms for MBN interpretation. By combining the predictive capability of the proposed simulation method to a new generation of magnetic sensors (local and directional), ideal experimental configuration can be proposed particularly useful for workshop practice. This work also belongs to a larger project with the final objective of using and interpreting MBN as a quantitative NDT tool for stress detection. The following steps include the development of more complex mechanical testing configurations such as compression or biaxial loadings for validation purpose, the introduction of temperature effects in the simulation of the $MBN_{energy}(H)$ hysteresis cycles, or the simulation of stress-dependent MBN raw signals by extending the method described in [46] to the stress influence.

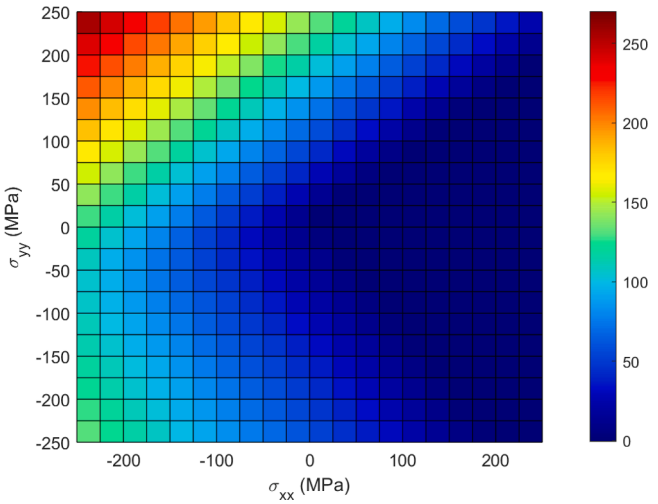

Fig. 14. FeCo alloy: Evolution of the predicted normalized H_{95} under biaxial stress states. The MBN sensor is positioned along σ_{xx} (RD).

Data availability statement

The raw/processed data required to reproduce these findings cannot be shared at this time due to technical or time limitations.

This research did not receive any specific grant from funding agencies in the public, commercial, or not-for-profit sectors.

Declaration of Competing Interest

The authors declare that they have no known competing financial interests or personal relationships that could have appeared to influence the work reported in this paper.

References

[1] P.J. Withers, H.K.D.H. Bhadeshia, Residual stress part 1—measurement techniques, Mater. Sci. Technol. 17 (4) (2001) 355–365.
[2] J. Guo, H. Fu, B.o. Pan, R. Kang, Recent Progress of Residual Stress Measurement Methods: A Review, Chin. J. Aeron. 34 (2) (2021) 54–78.
[3] American society for testing and materials; E837; Standard test method for determining residual stresses by the hole-drilling strain-gauge method, Pennsylvania: ASTM international, 2008.
[4] P. Pagliaro, M.B. Prime, H. Swenson, B. Zuccarello, Measuring Multiple Residual-Stress Components using the Contour Method and Multiple Cuts, Exp. Mech. 50 (2) (2010) 187–194.
[5] M.B. Prime, Residual stress measurement by successive extension of a slot: the crack compliance method, Appl. Mech. Rev. 52 (2) (1999) 75–96.
[6] C. Hellier, Handbook of non-destructive evaluation, McGraw-Hill, New York, 2003.
[7] R.E. Green, G. Dobmann, C.O. Ruud, P. Höller, "Nondestructive characterization of materials, in: Proceedings of the 3rd international symposium, Saarbrücken, FRG, 1988.
[8] W. Du, Y. Zhao, R. Roy, S. Add, L. Tinsley, A review of miniaturized Non-destructive Testing technologies for in-situ inspections, Procedia Manufacturing 16 (2018) 16–23.
[9] P. Höller, V. Hauk, G. Dobmann, C.O. Ruud, R.E. Green Jr, Nondestructive characterization of materials, in: Proceedings of the 3rd international symposium Saarbrücken, FRG, Oct 3-6, 1988.
[10] M.P. Blodgett, P.B. Nagy, Eddy current assessment of near-surface residual stress in shot peened nickel-base superalloys, J. Nondestruct. Eval. 23 (3) (2004) 107–123.
[11] F. Su, Methodology for the Stress Measurement of Ferromagnetic Materials by Using Magneto Acoustic Emission, Exp. Mech. 54 (8) (2014) 1431–1439.
[12] M. Shibata, K. Ono, Magnetomechanical acoustic emission — a new method for non-destructive stress measurement, NDT Int. 14 (5) (1981) 227–234.
[13] J. Gauthier, T.W. Krause, D.L. Atherton, Measurement of residual stress in steel using the magnetic Barkhausen noise technique, NDT & E International 31 (1) (1998) 23–31.
[14] M.R. Neyra Astudillo, M.I. López Pumarega, N.M. Núñez, A. Pochettino, J. Ruzzante, Magnetic Barkhausen noise and magneto acoustic emission in pressure vessel steel, J. Magn. Magn. Mater. 426 (2017) 779–784.
[15] D.M. Stewart, K.J. Stevens, A.B. Kaiser, Magnetic Barkhausen noise analysis of stress in steel, Curr. Appl. Phys. 4 (2-4) (2004) 308–311.

[16] J.W. Wilson, G.Y. Tian, V. Moorthy, B.A. Shaw, Magneto-Acoustic Emission and Magnetic Barkhausen Emission for Case Depth Measurement in En36 Gear Steel, IEEE Trans. Magn. 45 (1) (2009) 177–183.
[17] R.M. Bozorth, Magnetism, Enc. Brit. 14 (1957) 636–667.
[18] C. Kittel, Introduction to solid state physics, J. Wiley and sons Inc, New York, 1956.
[19] H. Sakamoto, M. Okada, M. Homma, Theoretical analysis of Barkhausen noise in carbon steels, IEEE Trans. Magn. 23 (5) (1987) 2236–2238.
[20] A.A. Samimi, T.W. Krause, L. Clapham, Multi-parameter Evaluation of Magnetic Barkhausen Noise in Carbon Steel, J. Nondestruct. Eval. 35 (3) (2016), https://doi.org/10.1007/s10921-016-0358-4.
[21] T.W. Krause, L. Clapham, D.L. Atherton, Characterization of the magnetic easy axis in pipeline steel using magnetic Barkhausen noise, J. Appl. Phys. 75 (1994) 7983–7988.
[22] B. Ducharne, M.Q. Le, G. Sebald, P.J. Cottinet, D. Guyomar, Y. Hebrard, Characterization and modeling of magnetic domain wall dynamics using reconstituted hysteresis loops from Barkhausen noise, J. Magn. Magn. Mater. 432 (2017) 231–238.
[23] P. Fagan, B. Ducharne, L. Daniel, A. Skarlatos, Multiscale modelling of the magnetic Barkhausen noise energy cycles, J. Magn. Magn. Mater. 517 (2021), 167395.
[24] B. Ducharne, B. Gupta, Y. Hebrard, J.B. Coudert, Phenomenological model of Barkhausen noise under mechanical and magnetic excitations, IEEE Trans. Magn. 54 (11) (2018) 1–6.
[25] C.W. Heaps, Magnetization of Nickel Under Compressive Stresses and the Production of Magnetic Discontinuities, Phys. Rev. 50 (2) (1936) 176–179.
[26] O. Ortega-Labra, T.L. Manh, P. Martinez-Ortiz, J.M. Hallen, J.A. Perez-Benitez, A novel system for non-destructive evaluation of surface stress in pipelines using rotational continuous magnetic Barkhausen noise, Meas.: J. Int. Meas. Conf. 136 (2019) 761–774.
[27] D.C. Jiles, W. Kiarie, An Integrated Model of Magnetic Hysteresis, the Magnetomechanical Effect, and the Barkhausen Effect, IEEE Trans. Magn. 57 (2) (2021) 1–11.
[28] J. Šrámek, M. Neslušan, F. Bahleda, K. Zgútová, P. Schenk, Influence of sample size and magnetizing voltage on Barkhausen noise during bending and uniaxial tensile tests, Acta Phys. Pol. A 137 (5) (2020) 640–643.
[29] V. Vengrinovich, D. Vintov, A. Prudnikov, P. Podugolnikov, V. Ryabtsev, Magnetic Barkhausen Effect in Steel Under Biaxial Strain/Stress: Influence on Stress Measurement, J. Nondestruct. Eval. 38 (2) (2019), https://doi.org/10.1007/s10921-019-0576-7.
[30] J.N. Mohapatra, A.K. Akela, Magnetic Evaluation of Tensile Deformation Behaviour of TRIP Assisted Steels, J. Nondestruct. Eval. 38 (1) (2019), https://doi.org/10.1007/s10921-019-0558-9.
[31] M. Roskosz, K. Fryczowski, Magnetic methods of characterization of active stresses in steel elements, J. Magn. Magn. Mater. 499 (2020) 166272, https://doi.org/10.1016/j.jmmm.2019.166272.
[32] J. Liu, G.Y. Tian, B. Gao, K. Zeng, Y. Zheng, J. Chen, Micro-macro characteristics between domain wall motion and magnetic Barkhausen noise under tensile stress, J. Magn. Magn. Mater. 493 (2020) 165719, https://doi.org/10.1016/j.jmmm.2019.165719.
[33] J.A. Avila, F.F. Conde, H.C. Pinto, J. Rodriguez, F.A.F. Grijalba, Microstructural and Residuals Stress Analysis of Friction Stir Welding of X80 Pipeline Steel Plates Using Magnetic Barkhausen Noise, J. Nondestruct. Eval. 38 (4) (2019), https://doi.org/10.1007/s10921-019-0625-2.
[34] J. Wu, C. Liu, E. Li, J. Zhu, S. Ding, Y. Wang, Motion-Induced Magnetic Barkhausen Noise for Evaluating Applied Stress in Pipelines, J. Nondestruct. Eval. 39 (4) (2020), https://doi.org/10.1007/s10921-020-00729-7.
[35] H. Dong, X. Liu, Y. Song, B.o. Wang, S. Chen, C. He, Quantitative evaluation of residual stress and surface hardness in deep drawn parts based on magnetic Barkhausen noise technology, Measurement 168 (2021) 108473, https://doi.org/10.1016/j.measurement.2020.108473.
[36] X. Zhang, J. Peng, X. Gao, J. Bai, J. Guo, Research on Stress Detection of DC01 Steel via Barkhausen Noise, Stud. Appl. Elect. Mech. 45 (2020) 152–158.
[37] J. Liu, G. Tian, B. Gao, K. Zeng, Y. Xu, Q. Liu, Time-Response-Histogram-Based Feature of Magnetic Barkhausen Noise for Material Characterization Considering Influences of Grain and Grain Boundary under In Situ Tensile Test, Sensors 21 (7) (2021), https://doi.org/10.3390/s21072350.
[38] A. Biesiekierski, K. Munir, Y. Li, C. Wen, 13 - Mechanical testing of metallic biomaterials, in: Metallic Biomaterials Processing and Medical Device Manufacturing, Elsevier, 2020, pp. 427–467, https://doi.org/10.1016/B978-0-08-102965-7.00013-8.
[39] P. Vourna, A. Ktena, E. Hristoforou, Residual Stress Analysis in Nonoriented Electrical Steel Sheets by Barkhausen Noise Measurements, IEEE Trans. Magn. 50 (4) (2014) 1–4.
[40] V. Moorthy, B.A. Shaw, P. Mountford, P. Hopkins, Magnetic Barkhausen emission technique for evaluation of residual stress alteration by grinding in case-carburised En36 steel, Act. Mat. 53 (19) (2005) 4997–5006.
[41] O. Kypris, I.C. Nlebedim, D.C. Jiles, Measuring stress variation with depth using Barkhausen signals, J. Magn. Magn. Mater. 407 (2016) 377–395.
[42] V. Vengrinovich, D. Dmitrovich, "Bi-axial stress quantitative evaluation with Barkhausen noise: the past and perspectives", proceeding of the 17th world conference on non-destructive testing, Shanghai, China, 2008.
[43] T.u. Le Manh, F. Caleyo, J.M. Hallen, J.H. Espina-Hernández, J.A. Pérez-Benitez, Model for the correlation between magnetocrystalline energy and Barkhausen noise in ferromagnetic materials, J. Magn. Magn. Mater. 454 (2018) 155–164.
[44] T. Le Manh, F. Caleyo, J.M. Hallen, J.P. Benítez, J.E. Hernández, Novel method for the accurate determination of magnetocrystalline energy from Barkhausen noise in ferromagnetic materials, Mater. Sci. Eng.: B 225 (2017) 98–107.
[45] B. Ducharne, Y.A. Tene Deffo, P. Tsafack, S.H. Nguedjang Kouakeuo, Directional Barkhausen noise magnetic measurement using the magnetic needle probe method, J. Magn. Magn. Mater. 519 (2021), 167453.
[46] P. Fagan, B. Ducharne, L. Daniel, A. Skarlatos, Magnetic Barkhausen noise: A simulation tool, AIP Adv. 11 (2) (2021) 025322, https://doi.org/10.1063/9.0000095.
[47] K. Matsumura, B. Fukuda, Recent developments of non-oriented electrical steel sheets, IEEE Trans. Mag. 20 (5) (1984) 1533–1538.
[48] O. Hubert, L. Daniel, Multiscale modeling of the magneto-mechanical behavior of grain-oriented silicon steels, J. Magn. Magn. Mater. 320 (2008) 1412–1422.
[49] F. Bloch, T. Waeckerle, H. Fraisse, The use of iron-nickel and iron-cobalt alloys in electrical engineering, and especially for electrical motors, in: 2007 Electrical Insulation Conference and Electrical Manufacturing *Expo*, 2007, pp. 394–401.
[50] M. Rekik, L. Daniel, O. Hubert, Equivalent stress model for magnetic hysteresis losses under biaxial loading, IEEE Trans. Mag. 50 (4) (2014) 1–4.
[51] M. Domenjoud, E. Berthelot, N. Galopin, R. Corcolle, Y. Bernard, L. Daniel, Characterization of giant magnetostrictive materials under static stress: influence of loading boundary conditions, Smart Mater. Struct. 28 (2019), 095012.
[52] A.J. Moses, H.V. Patel, P.I. Williams, AC Barkhausen noise in electrical steels: influence of sensing technique on interpretation of measurements, J. Electr. Eng. 57 (8) (2006) 3–8.
[53] T.W. Krause, L. Clapham, D.L. Atherton, Characterization of the magnetic easy axis in pipeline steel using magnetic Barkhausen noise, J. App. Phys. 75 (12) (1994) 7983–7988.
[54] C. Miguel, A.P. Zhukov, J. Gonzalez, Stress and/or field induced magnetic anisotropy in the amorphous $Fe_{73.5}Cu_1Nb_3Si_{15.5}B_7$ Alloy: Influence on the Coercivity, Saturation Magnetostriction and Magneto-Impedance Response, Phys. Stat. Sol. (a) 194 (1) (2002) 291–303.
[55] U. Aydin, P. Rasilo, F. Martin, D. Singh, L. Daniel, A. Belahcen, R. Kouhia, A. Arkkio, Modelling the effect of multi-axial stress on magnetic hysteresis of electrical steel sheets: a comparison, IEEE Trans. Mag. 53 (6) (2017) 2000904.
[56] R. Hu, A.-K. Soh, G.-P. Zheng, Y. Ni, Micromagnetic modeling studies on the effects of stress on magnetization reversal and dynamic hysteresis, J. of Mag and Mag. Mat. 301 (2) (2006) 458–468.
[57] L. Daniel, O. Hubert, N. Buiron, R. Billardon, Reversible magneto-elastic behavior: a multiscale approach, J. Mech. Phys. Solids 56 (2008) 1018–1042.
[58] L. Daniel, L. Bernard, O. Hubert, Multiscale Modeling of Magnetic Materials, in: A.-G. Olabi (Ed.), Encyclopedia of Smart Materials, vol. 5, Elsevier, Oxford, 2022, pp. 32–49.
[59] L. Daniel, M. Rekik, O. Hubert, A multiscale model for magneto-elastic behaviour including hysteresis effects, Arch. Appl. Mech. 84 (9) (2014) 1307–1323.
[60] M. Rekik, Mesure et modélisation du comportement magnéto-mécanique dissipatif des matériaux ferromagnétiques à haute limite élastique sous chargement multiaxial: application aux génératrices à grandes vitesses pour l'aéronautique, PhD, LMT ENS Cachan, 2014 in French.
[61] D.C. Jiles, D.L. Atherton, Theory of ferromagnetic hysteresis, J. Appl. Phys. 55 (6) (1984) 2115–2120.
[62] M.J. Sablik, G. Kwun, G.L. Burkhardt, Model for the effect of tensile and compressive stress on ferromagnetic hysteresis, J. Appl. Phys. 61 (8) (1987) 3799–3801.
[63] L. Bernard, L. Daniel, Effect of stress on magnetic hysteresis losses in a switched reluctance motor: Application to stator and rotor shrink fitting, IEEE Trans. Magn. 51 (9) (2015) 1–13.
[64] L. Bernard, B.J. Mailhe, S.L. Avila, L. Daniel, N.J. Batistela, N. Sadowski, Magnetic hysteresis under compressive stress: a multiscale-Jiles-Atherton approach, IEEE Trans. Magn. 56 (2) (2020) 1–4.
[65] B. Sai Ram, A.P.S. Baghel, S.V. Kulkarni, L. Daniel, I.C. Nlebedim, Inclusion of dynamic losses in a scalar magneto-elastic hysteresis model derived using multiscale and Jiles-Atherton approaches, IEEE Trans. Magn. 56 (3) (2020) 7510105.
[66] J. Wojewoda, A. Stefanski, M. Wiercigroh, T. Kapitaniak, Hysteretic effects of dry friction: modelling and experimental studies, Phil. Trans. Roy. Soc. A: Math., Phys. Eng. Sci. 366 (1866) (2008) 747–765.
[67] A. Bergqvist, Magnetic vector hysteresis model with dry friction-like pinning, Phys. B: Condensed Matter 233 (4) (1997) 342–347.
[68] B. Ducharne, D. Guyomar, G. Sébald, Low frequency modelling of hysteresis behaviour and dielectric permittivity in ferroelectric ceramics under electric field, J. Phys. D: Appl. Phys. 40 (2) (2007) 551–555.
[69] M. Rekik, O. Hubert, L. Daniel, H. Pfützner, G. Shilyashki, F. Hofbauer, Influence of a multi-axial stress on the reversible and irreversible magnetic behaviour of a 3% Si-Fe alloy, Int. J. Appl. Electromagn. Mech. 44 (3-4) (2014) 301–315.
[70] J. Pearson, P.T. Squire, M.G. Maylin, J.G. Gore, Apparatus for magnetic measurements under biaxial stress, IEEE Trans. Magn. 36 (5) (Sep. 2000) 3599–3601.
[71] V. Maurel, F. Ossart, Y. Marco, R. Billardon, Setup to test biaxial stress effect on magnetomechanic coupling, J. App. Phys. 93 (2003) 7115–7117.
[72] Y. Kai, Y. Tsuchida, T. Todaka, M. Enokizono, Influence of Biaxial Stress on Vector Magnetic Properties and 2-D Magnetostriction of a Nonoriented Electrical Steel

Sheet Under Alternating Magnetic Flux Conditions, IEEE Trans. Magn. 50 (4) (2014) 1–4.
[73] O. Hubert, F.S. Mballa-Mballa, S. He, S. Depeyre, Influence of Biaxial Stress on Magnetic Behavior of Dual-Phase Steel—Experiments and Modeling, IEEE Trans. Magn. 52 (5) (2016) 1–4.
[74] U. Aydin, P. Rasilo, F. Martin, A. Belahcen, L. Daniel, A. Haavisto, A. Arkkio, Effect of multi-axial stress on iron losses of electrical steel sheets, J. Magn. Magn. Mater. 469 (2019) 19–27.